GEOPHYSICS, VOL. 72, NO. 3 (MAY-JUNE 2007); P. S149–S154, 11 FIGS.
10.1190/1.2712113

Smoothing imaging condition for shot-profile migration

Antoine Guitton[1], Alejandro Valenciano[2], Dimitri Bevc[1], and Jon Claerbout[2]

ABSTRACT

Amplitudes in shot-profile migration can be improved if the imaging condition incorporates a division (deconvolution in the time domain) of the upgoing wavefield by the downgoing wavefield. This division can be enhanced by introducing an optimal Wiener filter which assumes that the noise present in the data has a white spectrum. This assumption requires a damping parameter, related to the signal-to-noise ratio, often chosen by trial and error. In practice, the damping parameter replaces the small values of the spectrum of the downgoing wavefield and avoids division by zero. The migration results can be quite sensitive to the damping parameter, and in most applications, the upgoing and downgoing wavefields are simply multiplied. Alternatively, the division can be made stable by filling the small values of the spectrum with an average of the neighboring points. This averaging is obtained by running a smoothing operator on the spectrum of the downgoing wavefield. This operation called the smoothing imaging condition. Our results show that where the spectrum of the downgoing wavefield is high, the imaging condition with damping and smoothing yields similar results, thus correcting for illumination effects. Where the spectrum is low, the smoothing imaging condition tends to be more robust to the noise level present in the data, thus giving better images than the imaging condition with damping. In addition, our experiments indicate that the parameterization of the smoothing imaging condition, i.e., choice of window size for the smoothing operator, is easy and repeatable from one data set to another, making it a valuable addition to our imaging toolbox.

INTRODUCTION

Shot-profile migration (SPM) algorithms based on one-way propagators generate kinematically accurate images of the subsurface. In many implementations, amplitudes are generally ignored within the imaging process, and are therefore considered fairly unreliable. However, obtaining accurate amplitudes is becoming crucial for Amplitude variation with angle (AVA) analysis or 4D processing. More important, accurate amplitudes can help unravel important geologic information that a simpler one-way propagator would not.

To obtain better amplitudes, three paths exist. First, the propagators used during the wavefield extrapolations need to be modified to include some amplitude information. This route has been explored by numerous authors (e.g., Wapenaar et al., 1999; Sava et al., 2001). For instance, Zhang et al. (2005b) show how the SPM algorithm can be modified to emulate WKBJ amplitudes.

Second, the imaging condition can be improved to yield better reflection coefficients. To reach this goal, Claerbout (1971) showed that the receiver wavefield needs to be divided by the source wavefield, making sure that division by zero does not occur. The imaging condition can also impact the spatial resolution of the final image (Valenciano and Biondi, 2003), as well as decrease imaging artifacts (Muijs et al., 2005). Often, however, the receiver and source wavefields are correlated because the parameterization of a stable division can be difficult.

Third, the imaging process can be cast as an inverse problem. For instance, least-squares migration with regularization has proved effective at improving amplitudes with incomplete surface data (Nemeth et al., 1999) and irregular subsurface illumination because of complex structures (e.g., Prucha et al., 1999; Kuehl and Sacchi, 2002). Because inversion is an expensive process, some strategies have been developed to approximate the Hessian (Plessix and Mulder, 2002; Rickett, 2003; Guitton, 2004) or estimate it on a target area only (Valenciano et al., 2006).

This paper presents a method for improving the imaging condition in SPM by approximating the division of the receiver wavefield by the source wavefield. This approximation consists of smoothing the denominator, as opposed to adding a stabilization parameter

Manuscript received by the Editor September 20, 2006; revised manuscript received January 8, 2007; published online April 6, 2007.
[1]3DGeo Inc., Santa Clara, California. E-mail: antoine@3dgeo.com; dimitri@3dgeo.com.
[2]Stanford University, Department of Geophysics, Stanford Exploration Project, Stanford, California. E-mail: valencia@sep.stanford.edu; jon@sep.stanford.edu.

(damping). In 2D, we illustrate this method with the Sigsbee2a and Pluto 1.5 data sets. In 3D, we present results obtained with the SEG/EAGE salt model data set, also known as C3-NA. These examples show that the smoothing imaging condition yields stronger amplitudes in areas of poor illumination and can image steeply dipping events better than the crosscorrelation imaging condition. An important property of the smoothing imaging condition is that it yields cleaner images than the damping imaging condition, where the noise level is high and the illumination is low. In addition, from a practical viewpoint, choosing a window size for the smoothing operator turns out to be much easier than choosing an adequate stabilization parameter for the division with damping.

THEORY

For shot-profile migration, an approximation of the reflection coefficient is given by (Claerbout, 1971)

$$\mathbf{I_{rc}}(\mathbf{x}) = \sum_{\mathbf{x_s}} \sum_{\omega} \frac{\mathbf{U}(\omega,\mathbf{x},\mathbf{x_s})}{\mathbf{D}(\omega,\mathbf{x},\mathbf{x_s})}, \tag{1}$$

where $\mathbf{x} = [x,y,z]$ is each image position, ω is the angular frequency, and $\mathbf{x_s} = [x_s,y_s,z_s]$ is each source position. Note that the upgoing ($\mathbf{U}$) and downgoing ($\mathbf{D}$) wavefields are also known as receiver and source wavefields, respectively. Physically, equation 1 states that a reflector exists where $\mathbf{U}$ and $\mathbf{D}$ coincide in time and space. Equation 1 will be unstable wherever $\mathbf{D}$ equals (or is close to) zero. For this reason, it is customary to multiply both the numerator and the denominator by the complex conjugate of $\mathbf{D}$ (i.e. $\mathbf{D}'$) and add a stabilization parameter ϵ as follows:

$$\mathbf{I_d}(\mathbf{x}) = \sum_{\mathbf{x_s}} \sum_{\omega} \frac{\mathbf{U}(\omega,\mathbf{x},\mathbf{x_s})\mathbf{D}'(\omega,\mathbf{x},\mathbf{x_s})}{\mathbf{D}(\omega,\mathbf{x},\mathbf{x_s})\mathbf{D}'(\omega,\mathbf{x},\mathbf{x_s}) + \epsilon}. \tag{2}$$

We call equation 2 the damping imaging condition. Note that equation 2 is equivalent to equation 1 multiplied by an optimal Wiener filter, assuming that the spectrum of the noise is white. This assumption breaks down when, for instance, residual multiples are present in the data. In theory, ϵ is related to the S/N. Similarly, the term within the two summations in equation 2 is the least-square inverse of the objective function $\mathbf{Q}$ (omitting $(\omega,\mathbf{x},\mathbf{x_s})$ for clarity) or

$$\mathbf{Q}(\mathbf{r}) = \|\mathbf{Dr} - \mathbf{U}\|^2 + \epsilon\|\mathbf{Ir}\|^2, \tag{3}$$

where $\mathbf{r}$ is the reflection coefficient and $\mathbf{I}$ the identity matrix. There are different ways to improve equation 2. Valenciano and Biondi (2003) proposed a 2D deconvolution scheme by summing over frequencies and source wavenumbers, thus increasing the resolution and decreasing the noise level of the migrated image (Muijs et al., 2005). The summations can be moved inside or outside the numerator and denominator (Plessix and Mulder, 2002; Zhang et al., 2005a). From an inversion point of view, better images can be obtained if regularization operators other than an identity matrix are used in equation 3.

Equation 2 poses a serious problem to practitioners: how do we estimate the damping parameter ϵ? One can envision many strategies based on the statistics of $\mathbf{D}(\omega,\mathbf{x},\mathbf{x_s})\mathbf{D}'(\omega,\mathbf{x},\mathbf{x_s})$. Alternatively, ϵ could be selected with a technique known as cross-validation, where different values of ϵ are selected and the residual power is plotted to form a characteristic L-shaped curve. When tuned correctly, these techniques can deliver very satisfying results. However, they are more difficult to use in a production environment in which robustness and reliability are often more important than mathematical accuracy. The imaging condition is usually estimated by crosscorrelating the downgoing ($\mathbf{D}$) and upgoing ($\mathbf{U}$) wavefields (Claerbout, 1971) as follows:

$$\mathbf{I_c}(\mathbf{x}) = \sum_{\mathbf{x_s}} \sum_{\omega} \mathbf{U}(\omega,\mathbf{x},\mathbf{x_s})\mathbf{D}'(\omega,\mathbf{x},\mathbf{x_s}). \tag{4}$$

We call equation 4 the crosscorrelation imaging condition. Jacobs (1982) analyzes in detail the differences between equations 4 and 2.

Smoothing imaging condition

We propose approximating the deconvolution imaging condition of equation 2. The main goal of this method is to emulate the deconvolution while being practical and robust. The main concept of this paper is to fill the zero of $\mathbf{D}(\omega,\mathbf{x},\mathbf{x_s})\mathbf{D}'(\omega,\mathbf{x},\mathbf{x_s})$ with neighboring points, as opposed to a more arbitrary constant value in equation 2. By "arbitrary," we mean that in effect, although being theoretically related to the S/N, ϵ is often chosen by trial and error. Therefore, we propose the following imaging condition:

$$\mathbf{I_s}(\mathbf{x}) = \sum_{\mathbf{x_s}} \sum_{\omega} \frac{\mathbf{U}(\omega,\mathbf{x},\mathbf{x_s})\mathbf{D}'(\omega,\mathbf{x},\mathbf{x_s})}{\langle \mathbf{D}(\omega,\mathbf{x},\mathbf{x_s})\mathbf{D}'(\omega,\mathbf{x},\mathbf{x_s})\rangle_{(x,y,z)}}, \tag{5}$$

where $\langle . \rangle_{(x,y,z)}$ stands for smoothing in the image space in the x, y, and z directions. We call equation 5 the smoothing imaging condition. The smoothing operator can be a rectangle, a triangle, a Gaussian function, etc. In this paper, a triangle function is used. Although not presented here, it would be worthwhile to study the behavior of the migration with respect to the shape of the smoothing operator. Filling the zero of a spectrum with neighboring values is not new: interpolation with prediction-error filters performs similarly. Although equation 2 can be derived analytically from least-squares or filtering theory, equation 5 can not. Our formulation merely assumes that

$$\langle \mathbf{D}(\omega,\mathbf{x},\mathbf{x_s})\mathbf{D}'(\omega,\mathbf{x},\mathbf{x_s})\rangle_{(x,y,z)} \approx \mathbf{D}(\omega,\mathbf{x},\mathbf{x_s})\mathbf{D}'(\omega,\mathbf{x},\mathbf{x_s}) + \epsilon. \tag{6}$$

The terms in equation 6 behave differently. Where $\mathbf{D}$ is strong, equation 2 converges to equation 1; in contrast, equation 5 does not, because all values will be smoothed. Now, when $\mathbf{D}$ is small, equation 2 converges to equation 4; in contrast, equation 5 fills the spectral holes with neighboring values. Therefore, for the smoothing imaging condition, we might expect better results than the damping imaging condition where $\mathbf{D}$ is weak, and lesser results where $\mathbf{D}$ is strong. Our results seem to indicate that even in the case of strong signal, the methods yield similar results, however.

For the smoothing imaging condition, only one parameter is needed, i.e., the size of the smoothing window $\mathbf{n} = [n_x,n_y,n_z]$. This parameter has more physical appeal than ϵ in equation 2 because we can choose it based on the frequency we are propagating or on the complexity of the model. For instance, although not done here, it seems reasonable to increase the size of the smoothing window with increasing frequency. Note that in all our results, we use a horizontal smoothing $\mathbf{n} = [n_x,n_y]$ only.

A look at the denominator

As an illustration of this method for a source at $x = 15.0$ km in the Sigsbee2a velocity model (Figure 1, we estimate the illumination maps $\mathbf{D}(\omega,\mathbf{x},\mathbf{x}_s)\mathbf{D}'(\omega,\mathbf{x},\mathbf{x}_s)$ at 5 (Figure 2a) and 45 Hz (Figure 3a). We also show the smoothed versions $\langle \mathbf{D}(\omega,\mathbf{x},\mathbf{x}_s)\mathbf{D}'(\omega,\mathbf{x},\mathbf{x}_s)\rangle_x$ in Figures 2b and 3b. We do not show the illumination map for $\mathbf{D}(\omega,\mathbf{x},\mathbf{x}_s)\mathbf{D}'(\omega,\mathbf{x},\mathbf{x}_s) + \epsilon$ because it would look identical to $\mathbf{D}(\omega,\mathbf{x},\mathbf{x}_s)\mathbf{D}'(\omega,\mathbf{x},\mathbf{x}_s)$ with a constant ϵ. In both Figures 2 and 3, red colors mean high values, whereas blue colors mean low values.

The effect of the smoothing is clear in Figures 2b and 3b. The smoothing retains the main illumination information while filling the zero. It also attenuates the strong variations of amplitude in the illumination paths of Figure 3a at 45 Hz. These patterns come from the destructive interference of waves traveling in different directions and are not related to the sampling of the velocity model. They might damage the final image if the imaging condition with damping (equation 2) is not parameterized correctly. Figures 2 and 3 illustrate also that low frequencies need small smoothing windows and that high frequencies need bigger ones (the same is true for ϵ in equation 2). In practice, however, because it would require more parameters, we opted for a single size for all the frequencies.

Better imaging conditions help correct amplitude in areas of poor illumination. They also help boost the amplitude of the migration operator at high dips. Figure 4 displays two impulse responses in a $v(z)$ medium using the crosscorrelation imaging condition (Figure 4a) and the smoothing imaging condition (Figure 4b). Dips close to 90° are stronger after division. This can have an important impact in the final image where faults and steep reflectors are present.

Size of the smoothing window

In the Sigsbee2a results, we selected a horizontal smoothing window of 4 km. As illustrated in the next sections, we select the same size for Pluto and a 3.2×3.2 km window for C3-NA. Remarkably, these numbers are essentially the same. Because we can learn from previous models, choosing the right size for $\mathbf{n}$ becomes more systematic and repeatable from one migration to the next.

Although not shown here, we conducted a series of tests to analyze the sensitivity of our results with respect to the size of the smoothing window. These results indicate that the migration result is quite robust to this parameter. Conducting similar tests with the damping imaging condition proved more challenging because we had to iterate several times before finding a satisfying ϵ. We compared how the image would evolve by decreasing both ϵ in equation 2 and $\mathbf{n}$ in equation 5; we noticed that the image deteriorates much faster with the damping imaging condition than with the smoothing imaging condition. Both results would eventually look the same for very small values of both ϵ and $\mathbf{n}$.

In the next section, we present migration results for three synthetic data sets. They illustrate that the smoothing imaging condition increases amplitudes in areas of poor illumination and yields similar results to the damping imaging condition. They also prove that amplitude of steeply dipping reflectors, such as faults, is improved.

EXAMPLES

In this section, we illustrate our imaging condition on two 2D data sets and on one 3D data set.

Migration of the Sigsbee2a data set

Figure 5 displays a comparison of three images obtained with three different imaging conditions. Compared to the crosscorrelation imaging condition of Figure 5a, both the damping (Figure 5b) and smoothing (Figure 5c) imaging conditions show balanced amplitude below the salt; they also look very similar, which indicates that the smoothing imaging condition is effectively correcting for illumination effects.

Looking at more details in Figure 6, we notice that the noise level is higher when the damping imaging condition is used. For instance, the strong reflector at $z = 4.6$ km appears discontinuous in Figure

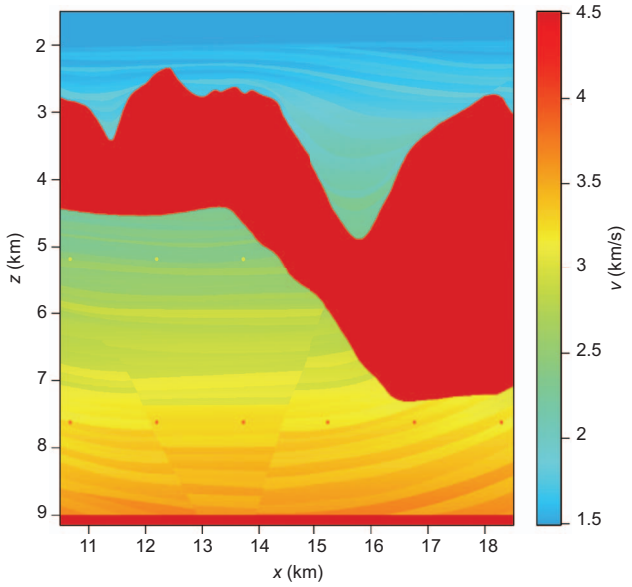

Figure 1. A close-up of the velocity model for the Sigsbee2a data set. Illumination maps are estimated for this model in Figures 2 and 3.

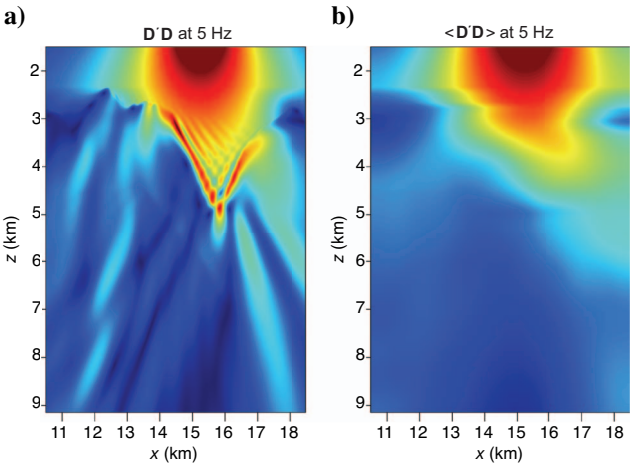

Figure 2. Illumination maps $\mathbf{D}'\mathbf{D}$ at 5 Hz (a) without and (b) with smoothing. Red colors correspond to high values, whereas blue colors correspond to low values. The size of the smoothing window is 4 km. The zero has been filled after smoothing. The patterns of interfering fringes come from the destructive interference of seismic waves traveling in different directions.

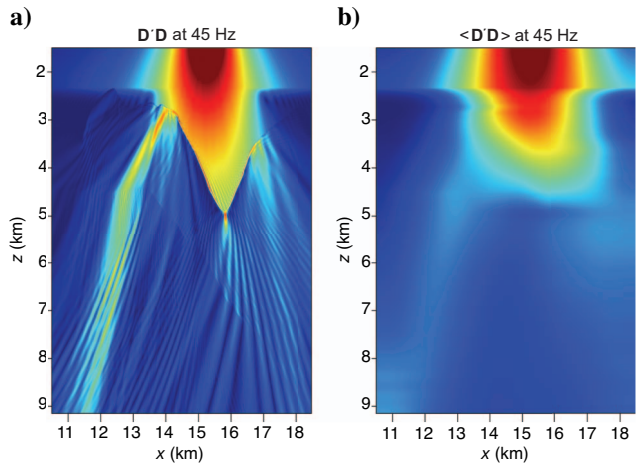

Figure 3. Illumination maps $\mathbf{D}'\mathbf{D}$ at 45 Hz (a) without and (b) with smoothing. Red colors correspond to high values, whereas blue colors correspond to low values. The size of the smoothing window is 4 km. The patterns of interfering fringes come from the destructive interference of seismic waves traveling in different directions.

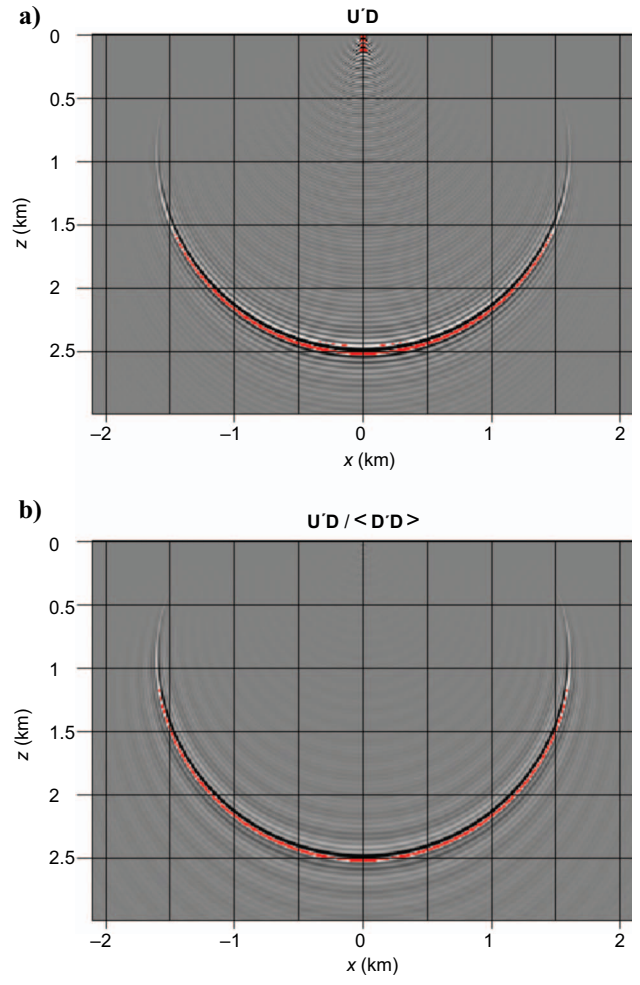

Figure 4. Impulse responses in a $v(z)$ medium for (a) the crosscorrelation imaging condition and (b) the smoothing imaging condition. The clipped values for each impulse are shown in red. High dips get higher amplitudes after division.

6b. As shown in Figure 6d, this discontinuity corresponds to a low value of the illumination map at 5 Hz. Although not shown here, this low illumination corridor is present for a wide range of frequencies. As anticipated, by using the smoothing imaging condition in Figure 6c, we obtain a better image. A higher ϵ for the damping imaging condition would mitigate this effect, but would also decrease the overall balancing effect of the division. One can also envision a space-varying ϵ; however; this option would probably require more parameters, something we want to avoid for practical reasons.

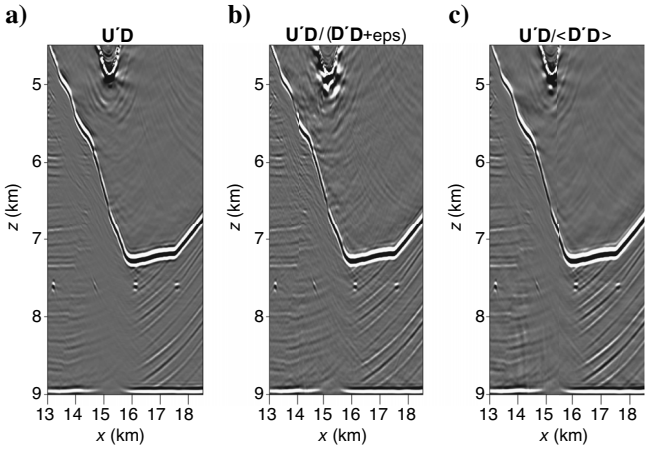

Figure 5. Migration results of the Sigsbee2a data set for (a) crosscorrelation imaging condition, (b) damping imaging condition ($\epsilon = 0.0001$), and (c) smoothing imaging condition. Amplitudes below the salt are balanced after division. Note that (b) and (c) are very similar.

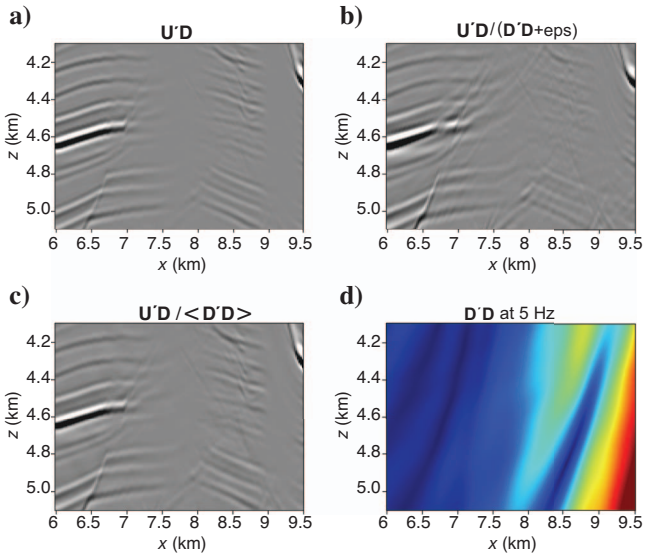

Figure 6. Close-up of the migration results of the Sigsbee2a data set for (a) crosscorrelation imaging condition, (b) damping imaging condition ($\epsilon = 0.0001$) and (c) smoothing imaging condition. Panel (d) shows the illumination map at 5 Hz. Red colors correspond to high values, whereas blue colors correspond to low values. The strong reflector in (a) at $z = 4.6$ km appears discontinuous when using the damping imaging condition. This discontinuity coincides with a very low value of $\mathbf{D}'\mathbf{D}$ in Figure 6d.

Migration of the Pluto 1.5 data set

Figures 7 and 8 display a comparison of three images obtained with three different imaging conditions. Similar to what we observed for the Sigsbee2a data set, areas of low illumination have stronger amplitudes when the damping and smoothing imaging conditions are used. In Figure 7, the steep flanks at z = 4.5 km are well imaged with both smoothing and damping. The flat reflector at z = 9 km shows more balanced amplitudes below the salt in both Figures 7 and 8.

These two 2D data examples illustrate two important aspects of the smoothing imaging condition: First, it yields images similar to that of the damping imaging condition. Second, it tends to have lower noise levels because the denominator of equation 5 is smooth at every frequency. In addition, the size of the smoothing window **n** is easy to select. In the next section, we illustrate the smoothing imaging condition on the C3-NA data set.

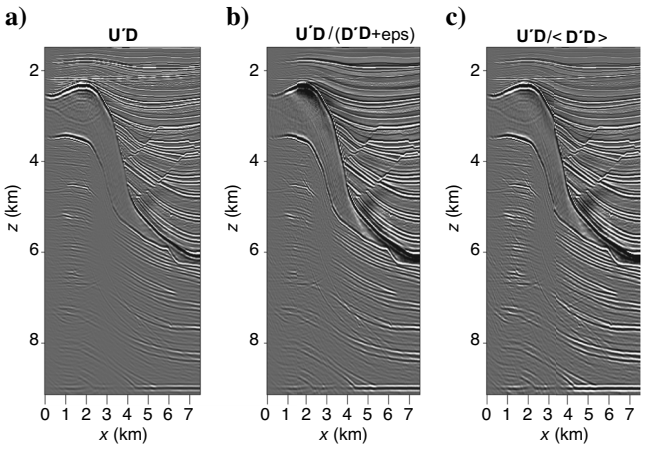

Figure 7. Migration results of the Pluto 1.5 data set for (a) crosscorrelation imaging condition, (b) damping imaging condition (ϵ = 0.001), and (c) smoothing imaging condition. The steep flanks are well imaged in (b) and (c).

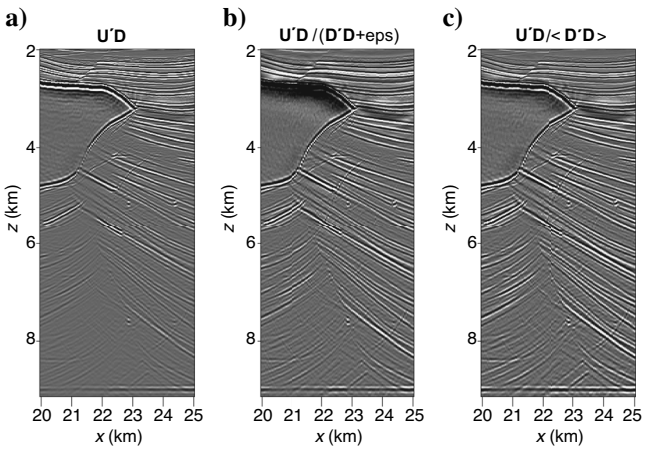

Figure 8. Migration results of the Pluto 1.5 data set for (a) crosscorrelation imaging condition, (b) damping imaging condition (ϵ = 0.001), and (c) smoothing imaging condition. The steep flanks are well imaged in (b) and (c). Areas of poor illumination below 5.0 km have stronger amplitudes in (b) and (c). Damping and smoothing yield similar results.

Migration of the C3-NA data set

Figure 9 shows a window of the velocity model for the migration results of Figures 10 and 11. For this example, because we proved in the 2D examples that the damping and smoothing imaging conditions yield similar results (except where the noise is strong and the illumination is low), we applied the crosscorrelation and smoothing imaging conditions only. In this example, we notice that the flat reflectors at $z \approx 3.5$ km have stronger amplitudes when the smoothing imaging condition is used. In addition, the salt flank at x = 6.0 km shows more balanced amplitudes.

One important effect of the smoothing imaging condition appears on the fault planes. The faults are stronger in Figure 11 than in Figure 10. Similar to Figure 4, steep dips get higher amplitudes, unraveling

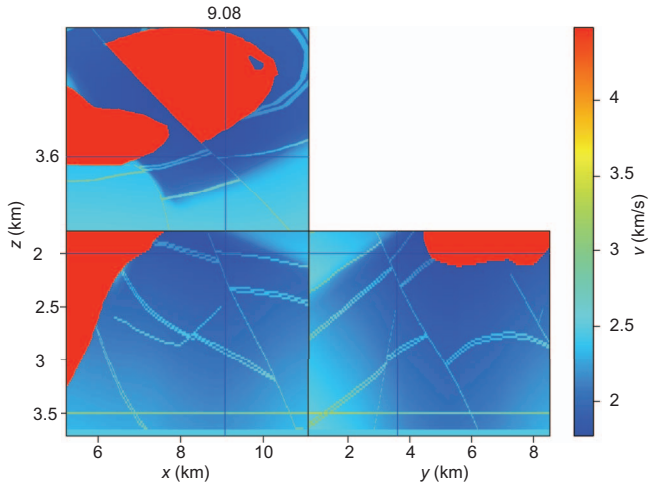

Figure 9. Velocity model for the C3 data set used in Figures 10 and 11. The top panel is a depth slice at z = 2.0 km, the center panel is a constant crossline slice at y = 3.6 km, and the right panel is a constant inline slice at x = 9.08 km. The lines show where these section intersect in the 3D volume.

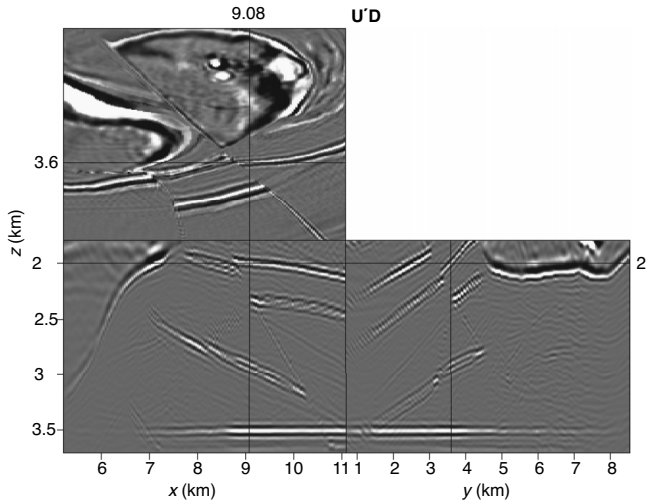

Figure 10. Migration result obtained with the crosscorrelation imaging condition. Both Figures 10 and 11 are scaled to one and displayed with the same clip (0.03).

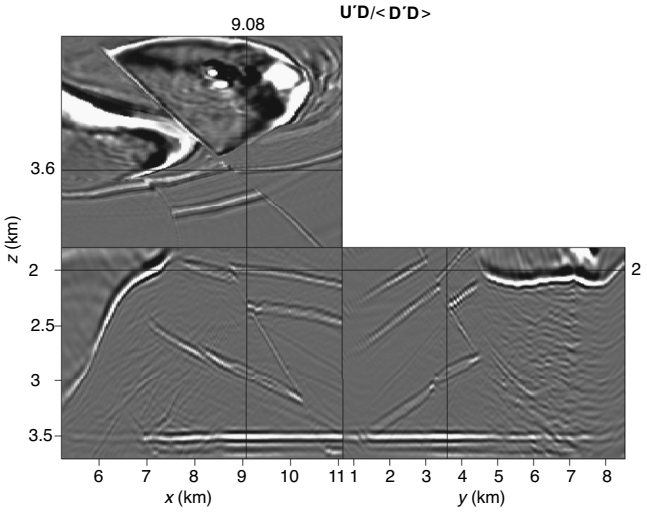

Figure 11. Migration result obtained with the smoothing imaging condition. Compared to Figure 10, the salt flanks and the flat reflector at the bottom of the image have stronger amplitudes. Faults that were weak in Figure 10 are well imaged. The subsalt area ($y \geq 5.0$ km) becomes noisier owing to a very poor illumination.

important geologic information. Note that kinematically the accuracy of the one-way propagator is not increased: we witness an amplitude effect only.

It is important to notice that having higher amplitudes for steeply dipping reflectors and for regions of low illumination might create problems if the S/N is small or if the velocity is not accurate. Figure 11 illustrates this point very well for $y \geq 5.0$ km. There, migration artifacts are boosted because of the lack of reflected energy in the subsalt area. In the inline panel, we also notice weak linear events parallel to the salt flank appearing after smoothing. Because of a poor illumination, noisy events, such as internal multiples, can affect our image because they are not incorporated into our noise model; in other words, their spectrum is not white. This important drawback is not specific to the smoothing imaging condition, however. It merely reflects some limitations of the division imaging condition with damping or smoothing.

CONCLUSION

We presented the smoothing imaging condition. At each frequency and for each shot, the image is divided by a smoothed version of the source illumination map, as opposed to a damped one. As exemplified in this paper, this imaging condition is superior to the damping imaging condition in three important aspects. First, the parameterization is very straightforward and physically appealing: we only need to decide on the size of the smoothing window **n**, which operates in the image space. Second, although not shown here, our experiments indicate that the migration result is quite robust to **n**. For instance, this parameter is almost equal for all the results presented here. Third, the smoothing imaging condition tends to decrease the noise level present in the damping imaging condition. This can be important for real data examples where the velocity model is not accurate.

ACKNOWLEDGMENTS

We thank Biondo Biondi for many useful suggestions during this work. Alejandro Valenciano and Jon Claerbout thank the sponsors of the Stanford Exploration Project for their financial support. The Sigsbee2a and Pluto 1.5 data sets were made available by the former members of the SMAART J.V.

REFERENCES

Claerbout, J. F., 1971, Toward a unified theory of reflector mapping: Geophysics, **36**, 467–481.
Guitton, A., 2004, Amplitude and kinematic corrections of migrated images for nonunitary imaging operators: Geophysics, **69**, 1017–1024.
Jacobs, A., 1982, The pre-stack migration of profiles: Ph.D. thesis, Stanford University.
Kuehl, H., and M. Sacchi, 2002, Robust AVP estimation using least-squares wave-equation migration: 72nd Annual International Meeting, SEG, Expanded Abstracts, 281–284.
Muijs, R., K. Holliger, and J. O. Robertsson, 2005, Prestack depth migration of primary and surface-related multiple reflections: 75th Annual International Meeting, SEG, Expanded Abstracts, 2107–2110.
Nemeth, T., C. Wu, and G. T. Schuster, 1999, Least-squares migration of incomplete reflection data: Geophysics, **64**, 208–221.
Plessix, R., and W. Mulder, 2002, Amplitude-preserving finite-difference migration based on a least-square formulation in the frequency domain: 72nd Annual International Meeting, SEG, Expanded Abstracts, 1212–1215.
Prucha, M., B. Biondi, and W. Symes, 1999, Angle-domain common image gathers by wave-equation migration: 69th Annual International Meeting, SEG, Expanded Abstracts, 824–827.
Rickett, J., 2003, Illumination-based normalization for wave-equation depth migration: Geophysics, **68**, 1371–1379.
Sava, P., B. Biondi, and S. Fomel, 2001, Amplitude-preserved common image gathers by wave-equation migration: 71st Annual International Meeting, SEG, Expanded Abstracts, 296–299.
Valenciano, A., and B. Biondi, 2003, 2D deconvolution imaging condition for shot profile migration: 73rd Annual International Meeting, SEG, Expanded Abstracts, 1059–1062.
Valenciano, A., B. Biondi, and A. Guitton, 2006, Target-oriented wave-equation inversion: Geophysics, **71**, no. 4, A35–A38.
Wapenaar, K., A. J. V. Wijngaarden, W. van Geloven, and T. van der Leij, 1999, Apparent AVA effects of fine layering: Geophysics, **64**, 1939–1948.
Zhang, Y., J. Sun, C. Notfors, S. H. Gray, L. Chernis, and J. Young, 2005a, Delayed-shot 3D depth migration: Geophysics, **70**, no. 5, E21–E28.
Zhang, Y., G. Zhang, and N. Bleistein, 2005b, Theory of true-amplitude one-way wave equations and true-amplitude common-shot migration: Geophysics, **70**, no. 4, E1–E10.